JACS
JOURNAL OF THE AMERICAN CHEMICAL SOCIETY
pubs.acs.org/JACS
Article

The Interplay between Luminescence Dissymmetry Factor and Quantum Yield: Symmetric and Asymmetric Hydrogen Bonding

Zhaoyu Wang, Xin Zeng, Wenkai Zhao, Yunchao Miao, Haolin Lu, Hebin Wang, Tianyin Shao, Xinyi Niu, Sehrish Gull, Tianjiao Qiao, Bing Sun, Xinfeng Liu, Hao-Li Zhang, Yongsheng Chen, and Guankui Long*

Cite This: J. Am. Chem. Soc. 2025, 147, 37771−37778
Read Online
ACCESS | Metrics & More | Article Recommendations | Supporting Information

ABSTRACT: Unraveling the luminescence−structure relationship in metal-free chiral perovskites remains challenging, particularly for achieving both a strong circularly polarized luminescence (CPL) and high photoluminescence quantum yield (PLQY). Here, we attempt to decode this hidden linkage by constructing the isomorphic polymorph-based metal-free chiral perovskite through the rational design of the A-site cation. The distinct steric hindrance between *meta*- and *ortho*-ammonium sites in 2-methylpiperazine-1,4-diium provides two possibilities for forming the hydrogen bond, which could control the crystallization pathways. Therefore, two different metal-free chiral perovskite polymorphs (A and B) with symmetric or asymmetric hydrogen bonding were obtained, which exhibit a remarkable difference in PLQY (36.51% vs 1.85%) and photoluminescence dissymmetry factor ($|g_{lum}|$, 0.032 vs 0.066). The highly luminescent polymorph A demonstrates stronger intermolecular coupling mediated by the symmetric hydrogen bonding, which effectively suppresses the nonradiative decay through rigidification of the octahedral framework, thereby enhancing the PLQY. In contrast, the asymmetric hydrogen bonding in polymorph B induces a greater structural distortion, which enhances the electron−phonon coupling and consequently reduces the PLQY. However, this asymmetric hydrogen bonding promotes efficient chirality transfer, leading to an increase of $|g_{lum}|$. Our work provides a molecular-level understanding of symmetric and asymmetric hydrogen bonding to determine the crystal packings and exciton dynamics, and thus the luminescence dissymmetry factor and quantum yield.

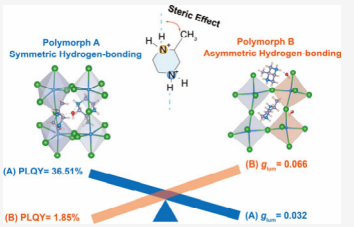

INTRODUCTION

The pursuit for sustainable optoelectronic materials has driven the development of purely organic perovskites,[1] which demonstrate enhanced molecular tunability and superior environmental compatibility compared to their heavy-metal-containing hybrid perovskites.[2,3] However, the introduction of chiral ammonium ions, while enabling the chiroptical functionalities,[4,5] leaves the relationship between chiral luminescent performance (e.g., circularly polarized luminescence, CPL) and emission efficiency (e.g., photoluminescence quantum yield, PLQY) unresolved.[6] The key challenge is to elucidate the intricate structure−property relationships that govern how molecular packings simultaneously enable both high PLQY and efficient CPL performance.[7,8]

Polymorphism inherently originates from divergent molecular packing modes and intermolecular interaction networks.[9,10] Comparative analysis of the spatial molecular arrangements across polymorphs provides direct insights into the competition and synergy among the weak interactions (e.g., hydrogen bonding, van der Waals forces).[11,12] Investigating the hydrogen-bonding effects on chiral perovskite polymorphs could unveil two pivotal mechanisms: (1) hydrogen bonding assists chirality transfer, which locks the molecular conformations via hydrogen-bonding networks and influences the degree of chirality transfer; (2) 3D hydrogen-bonding networks restrict the molecular vibrations: intermolecular forces and orientation govern the nonradiative efficiency through reducing the electron−phonon couplings.[13−15]

This study employs the isostructural polymorphs of 3D metal-free perovskites to decipher how hydrogen bonding is affected by the steric effects at *meta*- versus *ortho*-ammonium sites (Figures 1a and S1), governing the crystal packing motifs and exciton−phonon couplings, thereby dictating the trade-off between circularly polarized luminescence dissymmetry factor (g_{lum}) and photoluminescence quantum yield (Figure 1b). Specifically, the reduced steric effect at *meta*-positions extended the symmetric hydrogen bond networks, whereas the participation of crowded *ortho*-ammonium groups directs the localized asymmetric hydrogen bonding.[16−18] Through systematic investigation of each polymorph, it is found that polymorph A's symmetric 3D hydrogen-bonded architecture rigidifies the $[NH_4I_6]^{5-}$ emissive clusters via the O−H···I

Received: August 11, 2025
Revised: September 23, 2025
Accepted: September 24, 2025
Published: October 3, 2025

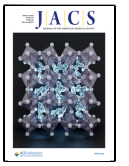

https://doi.org/10.1021/jacs.5c13847
J. Am. Chem. Soc. 2025, 147, 37771−37778

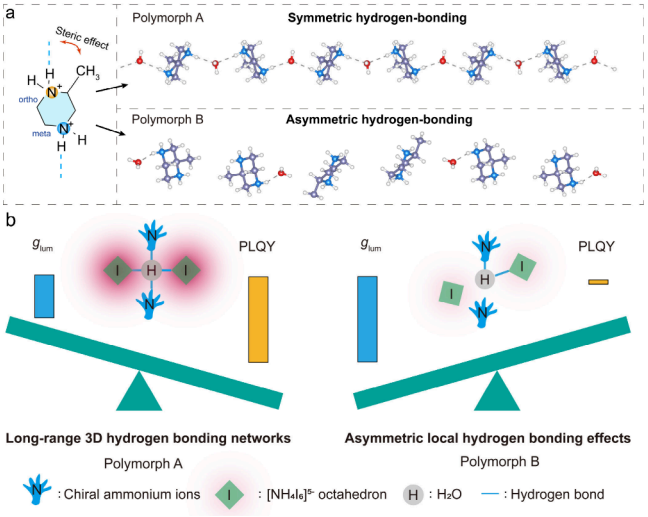

Figure 1. (a) The symmetric and asymmetric hydrogen bonding formed by the different ammonium sites owing to the steric hindrance, which induces polymorphs A and B. (b) Schematic illustration of the hydrogen-bonding topology-dependent trade-off between g_{lum} (chirality transfer) and PLQY (molecular rigidity).

interactions (1.5 Å), suppressing the vibrational dissipation and achieving a higher PLQY of 36.5%, which is one of the highest values among the reported chiral metal-free perovskites.[19,20] However, this structural order impedes efficient chirality transfer from chiral cations to the $[NH_4I_6]^{5-}$ octahedra, limiting the luminescence dissymmetry factor to 0.032. Conversely, polymorph B's asymmetric hydrogen bonding enhances the chirality transfer through a flexible lattice, elevating the g_{lum} to 0.066 at the cost of increased nonradiative decay (PLQY = 1.85%).[21] Therefore, achieving a high CPL brightness requires carefully balancing the competing factors that influence both PLQY and g_{lum}. Our work provides a molecular-level understanding on how to design the high-performance CPL emitter through rational tuning of the steric hindrance of chiral cations.

RESULTS AND DISCUSSION

In this study, we reported the successful crystallization of isostructural metal-free chiral perovskite crystals (identical molecular formula) with distinct crystalline polymorphs (*R*/*S*-2MP-NH_4I_3-$(H_2O)_{0.5}$, polymorphs A and B) using chiral 2-methylpiperazine-1,4-diium as the cations. A tailored crystallization protocol was developed through the antisolvent-assisted vapor diffusion, employing hydriodic acid as the solvent and diethyl ether as the antisolvent.[22−24] We identified two distinct crystalline phases: phase A displays a block-like morphology, while phase B exhibits a rod-like structure. The crystal structures of both phases were unambiguously determined through single-crystal X-ray diffraction analysis. The powder X-ray diffraction (PXRD) pattern of these metal-free perovskites agrees well with that simulated from their single-crystal data, further confirming their phase purity (Figures S2 and S3). Polymorph A (Sohncke space group of $P2_12_12_1$) exhibits a three-dimensional connectivity of $[NH_4I_6]^{5-}$ octahedra through corner-sharing (Figures S4, S5 and Tables S1, S2). Notably, the adjacent octahedra in polymorph A display distinct bond lengths (Table S3), corresponding to the distortion parameter (Δd) of 8.45 × 10^{-3} and 8.48 × 10^{-3}. In contrast, polymorph B (Sohncke space group of $P2_12_12$) shows significantly enhanced octahedral distortions, with Δd values escalating to 10.14 × 10^{-3} and 12.32 × 10^{-3}, respectively. We compared the total energies of their corresponding crystalline phases, revealing an energy difference of 7.73 kcal/mol between the two polymorphs (Figure S6). Subsequently, to elucidate the morphological differences between polymorphs A and B, the crystal surface free energy was calculated (Table S4). According to the Gibbs−Curie−Wulff theory, the normal growth rate of crystal planes is directly proportional to the surface free energy, expressed as γ_i/h_i = constant, where γ_i represents the specific surface free energy of crystal plane i, and h_i denotes the distance from the Wulff point. The distinct morphological evolution of polymorphs A (block-like) and B (rod-like) arises from the synergistic interplay between crystallographic facet energetics and geometric constraints. For polymorph A, multiple low-attachment-energy facets ({110}: E_{att} = −332.45 kcal/mol; {111}: E_{att} = −310.58 kcal/mol) impose balanced three-dimensional growth restrictions. This energy-equilibrated configuration drives the isotropic expansion, consistent with Wulff construction simulations showing a low growth anisotropy. In contrast, polymorph B exhibits strongly anisotropic growth kinetics

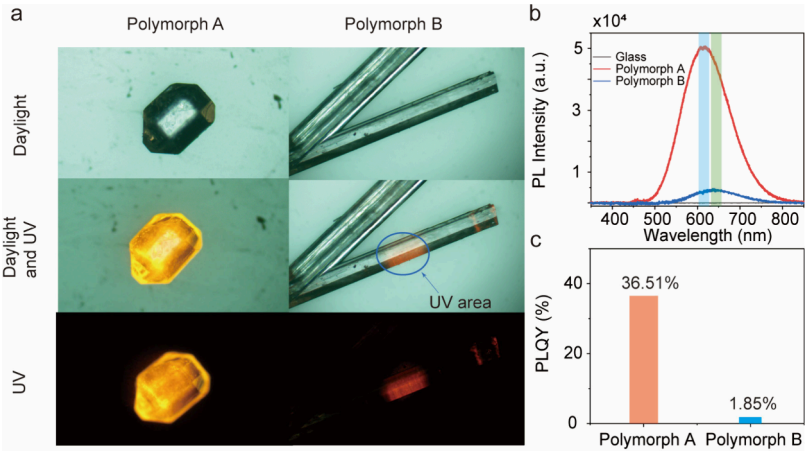

Figure 2. (a) Fluorescence microscopy image of polymorph A and polymorph B. (b) The steady-state PL spectrum of glass, polymorph A, and polymorph B. (c) The PLQY of polymorph A and polymorph B.

https://doi.org/10.1021/jacs.5c13847
J. Am. Chem. Soc. 2025, 147, 37771−37778

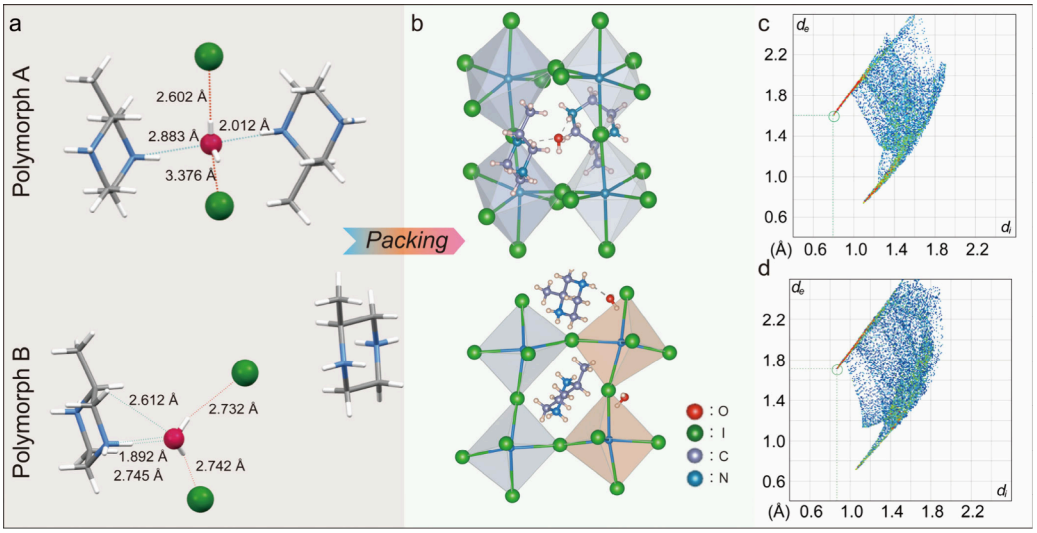

Figure 3. (a) Intermolecular interaction among H_2O, chiral cations, and I^- ions (top: polymorph A, bottom: polymorph B). (b) Packing diagrams of polymorph A (top) and polymorph B (bottom). (c) Two-dimensional Hirshfeld surface analysis fingerprint plots for the interactions of H_2O for polymorph A. (d) 2D Hirshfeld surface analysis fingerprint plots for the interactions of H_2O for polymorph B.

dominated by rapid elongation along the {200} direction (d_{hkl} = 13.94 Å, E_{att} = −151.05 kcal/mol), while the transverse growth is suppressed by the high-energy barrier facets ({011}: E_{att} = −339.65 kcal/mol). The extreme energy gradient (ΔE = 188.6 kcal/mol) and the preferential facet area distribution create a self-reinforcing growth dichotomy: the large interlayer spacing along the *a*-axis facilitates molecular stacking, whereas the tight atomic packing in lateral directions ({011} and {020}) restricts the radial growth. These results demonstrate that morphological control in metal-free perovskites can be rationally achieved through different facet selectivity, where the competing interactions between hydrogen bonding and van der Waals interactions dictate the supramolecular assembly (Figures S7, S8). Motivated by the pronounced structural discrepancies between polymorphs A and B, we have systematically investigated their structure-dependent photophysical properties and tried to establish their structure−property relationships.[25,26] This methodology elucidates how special crystalline architectures modulate the chirality transfer and radiative recombination through precise control of the structural distortion and supramolecular interactions.[27−29]

First, optical characterization through fluorescence microspectroscopy revealed the distinct photophysical behaviors between the two crystalline polymorphs. Polymorph A, exhibiting a block-like morphology, displayed an orange-red emission centered at 611 nm when excited at 330 nm. In contrast, polymorph B with rod-shaped crystals showed a red-shifted emission with a maximum at 640 nm under the identical excitation wavelength, accompanied by significantly reduced emission intensity (Figure 2b). Notably, as shown in Figures 2c and S9, photoluminescence quantum yield (PLQY) measurements of these different polymorphs uncovered a pronounced disparity: polymorph A demonstrated a 20-fold higher PLQY than that of polymorph B, highlighting the critical role of crystal morphology and packing in modulating the optoelectronic properties.

Despite their same structural formula, the different hydrogen-bonding modes are the primary origin of their distinct optoelectronic performances. In polymorph A, H_2O molecules mediate the hydrogen-bonding bridges between adjacent 2-methylpiperazine-1,4-diium cations (N−H···O and N···O: 2.012 and 2.883 Å), while forming strong O−H···I interactions with iodides (O−H···I: 2.602 and 3.376 Å, Figure 3a and Table S5), establishing a balanced and rigid 3D hydrogen-bonding network that effectively restricts the molecular vibrations. In contrast, polymorph B exhibits an asymmetric H_2O-cation-single-octahedron coordination mode. Specifically, H_2O molecules exclusively form hydrogen bonds with chiral cations on one side (N−H···O: 2.745 Å, C−H···O: 2.612 Å, and N−H···O: 1.892 Å). Unlike polymorph A, the two iodide ions in polymorph B engaged in the hydrogen bonding (O−H···I: 2.732 Å and 2.742 Å) originate from the same octahedron. This unique coordination topology reveals that H_2O acts as the molecular bridges for chirality transfer, which directionally propagates the structural asymmetry of chiral cations to one octahedron via asymmetric hydrogen-bonding networks, triggering the significant escalation of its distortion. Subsequently, this localized distortion propagates throughout the perovskite framework via cooperative corner-sharing effects (Figure 3b). Consequently, the asymmetric hydrogen-bonding in polymorph B enables the efficient modulation of the chiroptical activity through a dual mechanism: the asymmetric hydrogen bonding assisted chirality transfer and amplified cooperative distortion. Additionally, the energy framework calculations revealed that water molecules in polymorph A exhibit symmetric Coulombic interactions with the adjacent iodides (−0.9 kJ/mol per I^-, Figure S10), whereas in polymorph B, asymmetric interactions exist with two iodides of the same octahedron (−0.3 vs −0.1 kJ/mol, Figures S11, S12). These results further confirm that polymorphs A and B exhibit symmetric and asymmetric hydrogen bonding, respectively. The Hirshfeld surface analysis further confirms that stronger intermolecular interaction exists in polymorph A than polymorph B, as evidenced by the larger H···I (19.5% vs 18.5%) and O···H (30.8% vs 28.1%) proportion of interactions (Figures S13, S14). Notably, polymorph A demonstrates a shorter H···I contact (1.5 Å) that directly constrains the octahedral geometry (Figure 3c,d), whereas the weakened hydrogen-bonding constraints in polymorph B correlate well with the larger octahedral distortions as discussed above. In

https://doi.org/10.1021/jacs.5c13847
J. Am. Chem. Soc. 2025, 147, 37771−37778

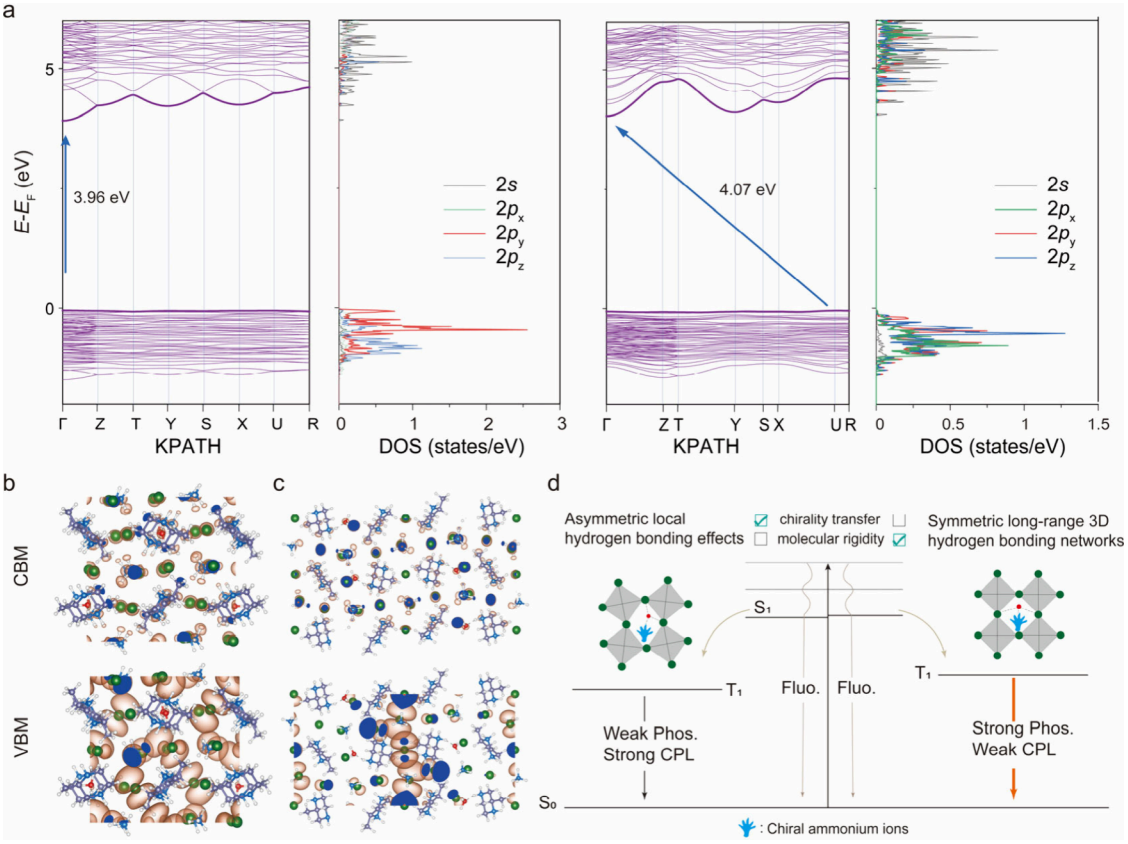

Figure 4. (a) Energy band structure and calculated partial density of states (PDOS) of polymorphs A and B. (b) Diagram of the charge density for the VBM and CBM for polymorph A. (c) A diagram of the charge density for the VBM and CBM for polymorph B. (d) Proposed mechanism of the luminescence process.

addition, polymorph B exhibits an extra H···N interaction (4.1%), which originates from the hydrogen bonding between chiral ammonium cations with H_2O, implying that H_2O acts as a bridge for stronger chirality transfer to the luminescent center. Crucially, the asymmetric hydrogen-bonding environments in polymorph B, where one octahedron acts as a dual hydrogen-bonding acceptor while the other one is unaffected by hydrogen-bonding, could induce an amplified distortion (Figure S15). Considering that the $[NH_4I_6]^{5-}$ cluster is the emission center, it is found that the octahedral distortions are governed by the strength of the hydrogen-bonding confinement. The rigid hydrogen bonding-network in polymorph A suppresses the nonradiative recombination through reducing the electron−phonon coupling, rationalizing its 20-fold enhanced PLQY compared to polymorph B (Table S6). Polymorph A exhibits a luminescence lifetime of 582.99 μs at 611 nm, while polymorph B shows a shorter lifetime of 385.62 μs at 640 nm (Figure S16). This trend aligns well with the crystal structures as discussed above and indicates that the symmetric 3D hydrogen-bonding networks indeed effectively suppress the phonon-assisted nonradiative decays. Temperature-dependent photoluminescence (PL) spectra reveal red-shifts exceeding 150 meV for both phases at low temperature compared to room temperature (159 meV for polymorph A and 176 meV for polymorph B, Figures S17, S18). This should originate from the stabilization of self-trapped excitons (STEs) formed through strong electron−phonon coupling, where lattice vibrations promote exciton localization into energetically favorable trapped states, thus giving rise to red-shifted STE emission at low temperatures. Furthermore, the observed 29 nm red-shift in emission from polymorph B (640 nm) relative to polymorph A (611 nm) suggests an efficient modulation of the electronic structures within the $[NH_4I_6]^{5-}$ chromophores. While the structural distortions account for the disparities of nonradiative loss, the spectral shift implies direct involvement of hydrogen-bonding networks in the orbital hybridization.

To confirm this hypothesis, we further investigated the electronic structures of these metal-free chiral perovskites through density functional theory (DFT) calculations. Polymorph A exhibits a direct bandgap of 3.96 eV at the Γ-point, whereas polymorph B demonstrates an indirect bandgap of 4.07 eV (Figure 4a). The calculated bandgaps of these two polymorphs are very close, which is also consistent with the experimental results based on the Tauc plot (Figure S19). Despite possessing a wider bandgap, polymorph B exhibits a red-shifted emission maximum at 640 nm versus 611 nm for polymorph A. This apparent bandgap-emission paradox originates from the indirect bandgap nature of polymorph B, which introduces two critical effects: (i) phonon-assisted radiative decays that are lower than the effective bandgap and (ii) enhanced nonradiative decay channels that preferentially depopulate the high-energy excitonic states. These combined effects ultimately lead to lower-energy photoluminescence despite the larger bandgap. Projected density of states (PDOS) analysis reveals distinct oxygen orbital participation in both systems. For polymorph A, the valence band maximum (VBM) is dominated by the $2p_y$ orbitals of the oxygen atom, while the conduction band minimum (CBM) arises exclusively from its $2s$ orbital (Figure S20). The VBM of polymorph B features

https://doi.org/10.1021/jacs.5c13847
J. Am. Chem. Soc. 2025, 147, 37771−37778

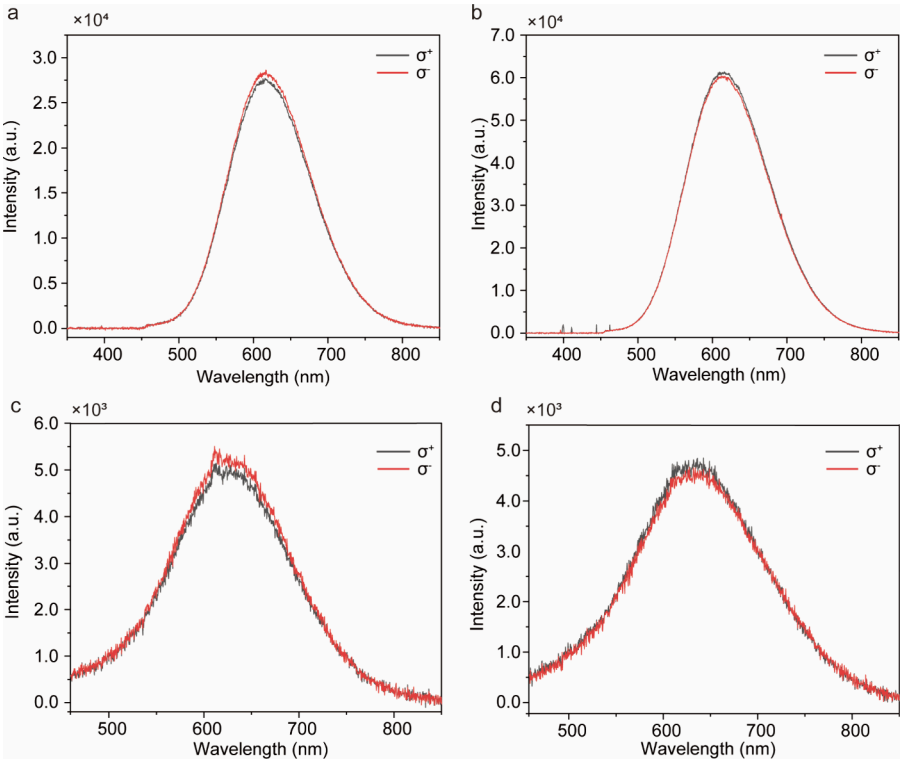

Figure 5. Polarization-resolved PL spectra of *R*/*S*-polymorph A (a and b) and *R*/*S*-polymorph B (c and d) microcrystals.

hybridized $2p_x$, $2p_y$, and $2p_z$ orbitals of oxygens, while its CBM is the same as that of polymorph A (Figure 4b and 4c). This marked divergence in VBM configurations confirms that distinct symmetric and asymmetric hydrogen bondings could modulate both electronic structures and emissive behaviors.

We then proposed a hydrogen-bonding-mediated exciton dynamics: for polymorph A, the 3D hydrogen-bonding network creates a rigid microenvironment through strong O−H···I interactions, effectively suppressing the $[NH_4I_6]^{5-}$ octahedral vibrations and nonradiative decays (Figure 4d). When it comes to polymorph B, the asymmetric hydrogen bonding facilitates the chirality transfer from chiral ammonium cations to the emissive octahedra, amplifying the lattice distortion and thus enhancing the CPL.

Notably, this rigidification originating from structural H_2O not only governs the radiative decay efficiency and bandgap but also profoundly tunes their chiroptical properties. The opposite CD signals for polymorphs A and B were observed (Figure S21). Then both polymorphs A and B were photoexcited by a linearly polarized laser, and the generated emission passed through a quarter waveplate, a Wollaston prism, to separate the right- and left-handed circularly polarized emission, which were simultaneously collected in different regions of the camera array (Figure 5). Polymorph A exhibits symmetric positive−negative CPL signals at 610 nm (Figure S22a). Similarly, polymorph B demonstrates mirror-symmetric CPL responses at 640 nm (Figure S22b). The anisotropy factor (g_{lum}), defined as $g_{lum} = 2(I_R - I_L)/(I_R + I_L)$, where I_R and I_L represent the right- and left-handed circularly polarized emission intensities, is then calculated.[30−32] It is found that polymorph B (low PLQY) displays a higher $|g_{lum}|$ value of 0.066, whereas polymorph A (high PLQY) shows a reduced $|g_{lum}|$ value of 0.032 (Figures S22c and S22d). This apparent paradox stems from the competitive interplay between molecular rigidity and chirality transfer.

In polymorph A, the 3D hydrogen-bonding network anchors the emissive $[NH_4I_6]^{5-}$ clusters within a rigid chiral framework via the O−H···I hydrogen bonding. While this geometric confinement could effectively suppress the electron−phonon coupling and increase the PLQY, the arrangement of chiral ammonium ions is relatively disordered, while the arrangement of the luminescent octahedral centers is relatively ordered in polymorph A, which implies a weaker chirality transfer from chiral ammonium cations to the luminescent centers. Conversely, for polymorph B, the chiral ammonium cation manifests relative order, while the octahedral centers exhibit enhanced aberrations and distortions, thereby indicating the stronger chirality transfer from the aforementioned chiral ammonium cations to the luminescent centers. Therefore, polymorph B exhibits an enhanced g_{lum} at the cost of reduced PLQY (1.85%), attributable to a more distorted crystal lattice. Our study demonstrates an inverse correlation between PLQY and g_{lum}, which provides an important molecular-level insight into the structure−property relationship of the metal-free chiral perovskites.

CONCLUSIONS

Our work unveils the pivotal role of symmetric and asymmetric hydrogen bonding in governing the trade-off between luminescent efficiency and dissymmetry factor in metal-free chiral perovskites. Through controlled crystallization, we isolated two isomorphic polymorphs (A/B) exhibiting inverse correlations between photoluminescence quantum yield (PLQY: 36.5% vs 1.85%) and circularly polarized luminescence dissymmetry factor ($|g_{lum}|$: 0.032 vs 0.066). Polymorph A features a 3D hydrogen-bonding network that rigidifies the $[NH_4I_6]^{5-}$ emissive clusters, suppressing the nonradiative

https://doi.org/10.1021/jacs.5c13847
J. Am. Chem. Soc. 2025, 147, 37771−37778

decay through O−H···I interactions, while limiting the chirality transfer through the disordered arrangements of chiral cations. Conversely, polymorph B's distorted octahedra and ordered chiral ammonium alignment enhance chirality transfer, amplifying the chiroptical properties at the cost of reducing the emission efficiency. Our findings establish a sustainable approach for designing metal-free perovskites with tunable chiroptical properties, effectively bridging the gap between molecular structure, luminescence dissymmetry factors, and quantum yield in metal-free chiral perovskites.

■ ASSOCIATED CONTENT

Supporting Information

The Supporting Information is available free of charge at https://pubs.acs.org/doi/10.1021/jacs.5c13847.

Reagents and materials, materials synthesis, instruments, theoretical calculations, PXRD patterns, crystal structures, PDOS, CD spectra, experimental bandgaps, the Hirshfeld surface analysis, energy framework calculations, simulated crystal morphology, temperature-dependent PL, time-resolved photoluminescence, PLQY, and crystal data table (PDF)

Accession Codes

Deposition Numbers 2453679−2453680, 2453897, and 2453899 contain the supplementary crystallographic data for this paper. These data can be obtained free of charge via the joint Cambridge Crystallographic Data Centre (CCDC) and Fachinformationszentrum Karlsruhe Access Structures service.

■ AUTHOR INFORMATION

Corresponding Author

Guankui Long − *Frontiers Science Center for New Organic Matter, Tianjin Key Lab for Rare Earth Materials and Applications, Renewable Energy Conversion and Storage Center (RECAST), National Institute for Advanced Materials, School of Materials Science and Engineering, Nankai University, Tianjin 300350, China;* orcid.org/0000-0002-1826-3736; Email: longgk09@nankai.edu.cn

Authors

Zhaoyu Wang − *Frontiers Science Center for New Organic Matter, Tianjin Key Lab for Rare Earth Materials and Applications, Renewable Energy Conversion and Storage Center (RECAST), National Institute for Advanced Materials, School of Materials Science and Engineering, Nankai University, Tianjin 300350, China*

Xin Zeng − *Frontiers Science Center for New Organic Matter, Tianjin Key Lab for Rare Earth Materials and Applications, Renewable Energy Conversion and Storage Center (RECAST), National Institute for Advanced Materials, School of Materials Science and Engineering, Nankai University, Tianjin 300350, China; CAS Key Laboratory of Standardization and Measurement for Nanotechnology, National Center for Nanoscience and Technology, Beijing 100190, China*

Wenkai Zhao − *Frontiers Science Center for New Organic Matter, Tianjin Key Lab for Rare Earth Materials and Applications, Renewable Energy Conversion and Storage Center (RECAST), National Institute for Advanced Materials, School of Materials Science and Engineering, Nankai University, Tianjin 300350, China*

Yunchao Miao − *Frontiers Science Center for New Organic Matter, Tianjin Key Lab for Rare Earth Materials and Applications, Renewable Energy Conversion and Storage Center (RECAST), National Institute for Advanced Materials, School of Materials Science and Engineering, Nankai University, Tianjin 300350, China;* orcid.org/0009-0007-8411-3705

Haolin Lu − *Frontiers Science Center for New Organic Matter, Tianjin Key Lab for Rare Earth Materials and Applications, Renewable Energy Conversion and Storage Center (RECAST), National Institute for Advanced Materials, School of Materials Science and Engineering, Nankai University, Tianjin 300350, China*

Hebin Wang − *Frontiers Science Center for New Organic Matter, Tianjin Key Lab for Rare Earth Materials and Applications, Renewable Energy Conversion and Storage Center (RECAST), National Institute for Advanced Materials, School of Materials Science and Engineering, Nankai University, Tianjin 300350, China*

Tianyin Shao − *Frontiers Science Center for New Organic Matter, Tianjin Key Lab for Rare Earth Materials and Applications, Renewable Energy Conversion and Storage Center (RECAST), National Institute for Advanced Materials, School of Materials Science and Engineering, Nankai University, Tianjin 300350, China*

Xinyi Niu − *Frontiers Science Center for New Organic Matter, Tianjin Key Lab for Rare Earth Materials and Applications, Renewable Energy Conversion and Storage Center (RECAST), National Institute for Advanced Materials, School of Materials Science and Engineering, Nankai University, Tianjin 300350, China*

Sehrish Gull − *Frontiers Science Center for New Organic Matter, Tianjin Key Lab for Rare Earth Materials and Applications, Renewable Energy Conversion and Storage Center (RECAST), National Institute for Advanced Materials, School of Materials Science and Engineering, Nankai University, Tianjin 300350, China*

Tianjiao Qiao − *Frontiers Science Center for New Organic Matter, Tianjin Key Lab for Rare Earth Materials and Applications, Renewable Energy Conversion and Storage Center (RECAST), National Institute for Advanced Materials, School of Materials Science and Engineering, Nankai University, Tianjin 300350, China*

Bing Sun − *State Key Laboratory of Natural Product Chemistry, Key Laboratory of Special Function Materials and Structure Design (MOE), College of Chemistry and Chemical Engineering, Lanzhou University, Lanzhou 730000, China;* orcid.org/0000-0002-6489-8345

Xinfeng Liu − *CAS Key Laboratory of Standardization and Measurement for Nanotechnology, National Center for Nanoscience and Technology, Beijing 100190, China;* orcid.org/0000-0002-7662-7171

Hao-Li Zhang − *State Key Laboratory of Natural Product Chemistry, Key Laboratory of Special Function Materials and Structure Design (MOE), College of Chemistry and Chemical Engineering, Lanzhou University, Lanzhou 730000, China;* orcid.org/0000-0002-6322-5202

Yongsheng Chen − *State Key Laboratory and Institute of Element-Organic Chemistry, Frontiers Science Center for New Organic Matter, The Centre of Nanoscale Science and Technology and Key Laboratory of Functional Polymer Materials, Renewable Energy Conversion and Storage Center*

(RECAST), College of Chemistry, Nankai University, Tianjin 300071, China; orcid.org/0000-0003-1448-8177

Complete contact information is available at: https://pubs.acs.org/10.1021/jacs.5c13847

Notes

The authors declare no competing financial interest.

■ ACKNOWLEDGMENTS

The authors gratefully acknowledge the financial sup-port from the NSFC (Grant Numbers: 52473305, 92256202, U22A20399, 12261131500, 22405111) of China, the Fundamental Research Funds for the Central Universities, Nankai University (Grant Number: 023-63233038), the 111 Project (B18030), and the Supercomputing Center of Lanzhou University.

■ REFERENCES

(1) Choi, H. S.; Lin, J.; Wang, G.; Wong, W. P. D.; Park, I.-H.; Lin, F.; Yin, J.; Leng, K.; Lin, J.; Loh, K. P. Molecularly thin, two-dimensional all-organic perovskites. *Science* **2024**, *384*, 60−66.

(2) Ye, H.-Y.; Tang, Y.-Y.; Li, P.-F.; Liao, W.-Q.; Gao, J.-X.; Hua, X.-N.; Cai, H.; Shi, P.-P.; You, Y.-M.; Xiong, R.-G. Metal-free three-dimensional perovskite ferroelectrics. *Science* **2018**, *361*, 151−155.

(3) Long, G.; Sabatini, R.; Saidaminov, M. I.; Lakhwani, G.; Rasmita, A.; Liu, X.; Sargent, E. H.; Gao, W. *Chiral-perovskite optoelectronics. Nat. Rev. Mater.* **2020**, *5*, 423−439.

(4) Peng, G.; Li, Z.; Xu, Y.; Lei, Y.; Wang, H.; Jin, Z. Evidence of Cation Symmetry Reduction Induced Bulk Photovoltaic Effect in Metal-Free Perovskite for Efficient Self-Powered X-Ray Detection. *Adv. Mater.* **2025**, *37*, 2502335.

(5) Song, X.; Hodes, G.; Zhao, K.; Liu, S. Metal-Free Organic Halide Perovskite: A New Class for Next Optoelectronic Generation Devices. *Adv. Energy Mater.* **2021**, *11*, 2003331.

(6) Wang, Z.; Lu, H.; Zhao, W.; Wang, H.; He, T.; Shao, T.; Niu, X.; Qiao, T.; Gull, S.; Miao, Y.; Sun, B.; Zhang, H.-L.; Chen, Y.; Long, G. Against the Wallach's Rule Through Rational Design of Metal-Free Chiral Perovskites Toward Efficient Red Circularly Polarized Phosphorescence. *Angew. Chem., Int. Ed.* **2025**, *64*, No. e202501360.

(7) Li, J.; Luo, Q.; Wei, J.; Zhou, L.; Chen, P.; Luo, B.; Chen, Y.; Pang, Q.; Zhang, J. Z. Circularly Polarized Luminescence Induced by Hydrogen-Bonding Networks in a One-Dimensional Hybrid Manganese(II) Chloride. *Angew. Chem., Int. Ed.* **2024**, *63*, No. e202405310.

(8) Wei, Y.; Li, C.; Li, Y.; Luo, Z.; Wu, X.; Liu, Y.; Zhang, L.; He, X.; Wang, W.; Quan, Z. Circularly Polarized Luminescence from Zero-Dimensional Hybrid Lead-Tin Bromide with Near-Unity Photoluminescence Quantum Yield. *Angew. Chem., Int. Ed.* **2022**, *61*, No. e202212685.

(9) Zhang, M.-M.; Zhang, R.; Yang, S.-Y.; Dong, X.-Y.; Zhang, C.; Si, Y.; Jia, T.; Han, Z.; Zang, S.-Q.; Mak, T. C. W. Assembling Octahedral Pt_2Ag_4 Clusters for High-Efficiency Circularly Polarized Luminescence. *Adv. Mater.* **2025**, *37*, 2502899.

(10) Li, W.; Huang, Q.; Mao, Z.; Zhao, J.; Wu, H.; Chen, J.; Yang, Z.; Li, Y.; Yang, Z.; Zhang, Y.; Aldred, M. P.; Chi, Z. Selective Expression of Chromophores in a Single Molecule: Soft Organic Crystals Exhibiting Full-Colour Tunability and Dynamic Triplet-Exciton Behaviours. *Angew. Chem., Int. Ed.* **2022**, *59*, 3739−3745.

(11) Chen, J.; Wei, Z.; Shan, Y.; Chen, S.; Wu, Z.; Liu, S.; Zhang, J.; Chen, X.; Liu, B. Bottom-Up Selective Growth of Ultralong Organic Phosphorescence Nanocrystals with Optimized Crystal Forms for In Vivo Optical Imaging. *Adv. Mater.* **2025**, *37*, 2418795.

(12) Bremner, C. A.; Simpson, M.; Harrison, W. T. A. New Molecular Perovskites: Cubic $C_4N_2H_{12}{\cdot}NH_4Cl_3{\cdot}H_2O$ and 2-H Hexagonal $C_6N_2H_{14}{\cdot}NH_4Cl_3$. *J. Am. Chem. Soc.* **2002**, *124*, 10960−10961.

(13) Li, Z.; Peng, G.; Chen, H.; Shi, C.; Li, Z.; Jin, Z. Metal-Free PAZE-$NH_4X_3{\cdot}H_2O$ Perovskite for Flexible Transparent X-ray Detection and Imaging. *Angew. Chem., Int. Ed.* **2022**, *61*, No. e202207198.

(14) Li, Q.; Zhou, M.; Yang, M.; Yang, Q.; Zhang, Z.; Shi, J. Induction of long-lived room temperature phosphorescence of carbon dots by water in hydrogen-bonded matrices. *Nat. Commun.* **2018**, *9*, 734.

(15) Bian, L.; Shi, H.; Wang, X.; Ling, K.; Ma, H.; Li, M.; Cheng, Z.; Ma, C.; Cai, S.; Wu, Q.; Gan, N.; Xu, X.; An, Z.; Huang, W. Simultaneously Enhancing Efficiency and Lifetime of Ultralong Organic Phosphorescence Materials by Molecular Self-Assembly. *J. Am. Chem. Soc.* **2018**, *140*, 10734−10739.

(16) Purdum, G. E.; Telesz, N. G.; Jarolimek, K.; Ryno, S. M.; Gessner, T.; Davy, N. C.; Petty, A. J., II; Zhen, Y.; Shu, Y.; Facchetti, A.; Collis, G. E.; Hu, W.; Wu, C.; Anthony, J. E.; Weitz, R. T.; Risko, C.; Loo, Y.-L. Presence of Short Intermolecular Contacts Screens for Kinetic Stability in Packing Polymorphs. *J. Am. Chem. Soc.* **2018**, *140*, 7519−7525.

(17) Larrégola, S. A.; Alonso, J. A.; Sheptyakov, D.; Algueró, M.; Muñoz, A.; Pomjakushin, V.; Pedregosa, J. C. An Original Polymorph Sequence in the High-Temperature Evolution of the Perovskite Pb_2TmSbO_6. *J. Am. Chem. Soc.* **2010**, *132*, 14470−14480.

(18) Chen, X.; Zhang, J.; Thind, A. S.; Sharma, S.; LaBollita, H.; Peterson, G.; Zheng, H.; Phelan, D. P.; Botana, A. S.; Klie, R. F.; Mitchell, J. F. Polymorphism in the Ruddlesden-Popper Nickelate $La_3Ni_2O_7$: Discovery of a Hidden Phase with Distinctive Layer Stacking. *J. Am. Chem. Soc.* **2024**, *146*, 3640−3645.

(19) Liang, L. Y.; Chen, B. B.; Gao, Y. T.; Lv, J.; Liu, M. L.; Li, D. W. Aqueous Solution Enhanced Room Temperature Phosphorescence through Coordination-Induced Structural Rigidity. *Adv. Mater.* **2024**, *36*, 2308180.

(20) Dai, X.-Y.; Huo, M.; Liu, Y. Phosphorescence resonance energy transfer from purely organic supramolecular assembly. *Nat. Rev. Chem.* **2023**, *7*, 854−874.

(21) Zhang, Y.; Qin, X.; Zhu, X.; Liu, M.; Guo, Y.; Zhang, Z. Direct observation of long-range chirality transfer in a self-assembled supramolecular monolayer at interface in situ. *Nat. Commun.* **2022**, *13*, 7737.

(22) Wu, H.-S.; Murti, B. T.; Singh, J.; Yang, P.-K.; Tsai, M.-L. Prospects of Metal-Free Perovskites for Piezoelectric Applications. *Adv. Sci.* **2022**, *9*, 2104703.

(23) Zhang, H.; Xu, Z.-K.; Wang, Z.-X.; Yu, H.; Lv, H.-P.; Li, P.-F.; Liao, W.-Q.; Xiong, R.-G. Large Piezoelectric Response in a Metal-Free Three-Dimensional Perovskite Ferroelectric. *J. Am. Chem. Soc.* **2023**, *145*, 4892−4899.

(24) Choi, H. S.; Li, S.; Park, I.-H.; Liew, W. H.; Zhu, Z.; Kwon, K. C.; Wang, L.; Oh, I.-H.; Zheng, S.; Su, C.; Xu, Q.-H.; Yao, K.; Pan, F.; Loh, K. P. Tailoring the coercive field in ferroelectric metal-free perovskites by hydrogen bonding. *Nat. Commun.* **2022**, *13*, 794.

(25) Mizoguchi, H.; Woodward, P. M.; Byeon, S.-H.; Parise, J. B. Polymorphism in $NaSbO_3$: Structure and Bonding in Metal Oxides. *J. Am. Chem. Soc.* **2004**, *126*, 3175−3184.

(26) Inaguma, Y.; Tanaka, K.; Tsuchiya, T.; Mori, D.; Katsumata, T.; Ohba, T.; Hiraki, K.-i.; Takahashi, T.; Saitoh, H. Synthesis, Structural Transformation, Thermal Stability, Valence State, and Magnetic and Electronic Properties of $PbNiO_3$ with Perovskite- and $LiNbO_3$-Type Structures. *J. Am. Chem. Soc.* **2011**, *133*, 16920−16929.

(27) Bang, J.; Matsuishi, S.; Hiraka, H.; Fujisaki, F.; Otomo, T.; Maki, S.; Yamaura, J.-i.; Kumai, R.; Murakami, Y.; Hosono, H. Hydrogen Ordering and New Polymorph of Layered Perovskite Oxyhydrides: $Sr_2VO_{4-x}H_x$. *J. Am. Chem. Soc.* **2014**, *136*, 7221−7224.

(28) Sun, Q.; Chen, W.; Ding, N.; Zhao, C.; Jiang, Z.; Li, S.; Pang, S. Unraveling the direct effect of hydrogen bonding on density and thermostability of energetic materials through isomerism. *Chem. Eng. J.* **2022**, *444*, 136539.

(29) Song, X.; Wang, Y.; Wang, C.; Wang, D.; Zhuang, G.; Kirlikovali, K. O.; Li, P.; Farha, O. K. Design Rules of Hydrogen-

Bonded Organic Frameworks with High Chemical and Thermal Stabilities. *J. Am. Chem. Soc.* **2022**, *144*, 10663−10687.
(30) Sun, M.-E.; Wang, F.; He, M.; Yang, Y.-N.; Yang, J.-K.; Zhu, M.-J.; Wan, Q.-Y.; Chen, G.; Wang, Y.; Fu, Y.; Li, Q.; Wang, Z.; Jiang, L.; Wu, Y.; Zang, S.-Q. Pressure-Driven Circularly Polarized Luminescence Enhancement and Chirality Amplification. *J. Am. Chem. Soc.* **2025**, *147*, 10706−10714.
(31) Feng, H.; Lan, X.; Feng, Z.; Chen, S.; Zhang, L.; Gao, H.; Han, C.; Chen, X.; Jiang, Q.; Meng, Z.; Lei, Y. An Alloy Engineering Strategy toward Helical Microstructures of Achiral π-Conjugated Molecules for Circularly Polarized Luminescence. *J. Am. Chem. Soc.* **2025**, *147*, 9250−9260.
(32) Jing, S.-M.; Gu, Z.-G.; Zhang, J. Chiral Cross-Linked Covalent Organic Framework Films for Highly Sensitive Circularly Polarized Luminescence Probing. *J. Am. Chem. Soc.* **2025**, *147*, 8948−8958.

https://doi.org/10.1021/jacs.5c13847
J. Am. Chem. Soc. 2025, 147, 37771−37778